Electrically induced 2D half-metallic antiferromagnets and spin field effect transistors

Shi-Jing Gong[a,b,1,2], Cheng Gong[c,d,1,2], Yu-Yun Sun[a], Wen-Yi Tong[a], Chun-Gang Duan[a,b], Jun-Hao Chu[a], and Xiang Zhang[c,d,2]

[a]Key Laboratory of Polar Materials and Devices, Ministry of Education, Department of Electronic Engineering, East China Normal University, Shanghai 200062, China; [b]Collaborative Innovation Center of Extreme Optics, Shanxi University, Taiyuan, Shanxi 030006, China; [c]Nanoscale Science and Engineering Center, University of California, Berkeley, CA 94720; and [d]Materials Sciences Division, Lawrence Berkeley National Laboratory, Berkeley, CA 94720

Engineering the electronic band structure of material systems enables the unprecedented exploration of new physical properties that are absent in natural or as-synthetic materials. Half metallicity, an intriguing physical property arising from the metallic nature of electrons with singular spin polarization and insulating for oppositely polarized electrons, holds a great potential for a 100% spin-polarized current for high-efficiency spintronics. Conventionally synthesized thin films hardly sustain half metallicity inherited from their 3D counterparts. A fundamental challenge, in systems of reduced dimensions, is the almost inevitable spin-mixed edge or surface states in proximity to the Fermi level. Here, we predict electric field-induced half metallicity in bilayer A-type antiferromagnetic van der Waals crystals (i.e., intralayer ferromagnetism and interlayer antiferromagnetism), by employing density functional theory calculations on vanadium diselenide. Electric fields lift energy levels of the constituent layers in opposite directions, leading to the gradual closure of the gap of singular spin-polarized states and the opening of the gap of the others. We show that a vertical electrical field is a generic and effective way to achieve half metallicity in A-type antiferromagnetic bilayers and realize the spin field effect transistor. The electric field-induced half metallicity represents an appealing route to realize 2D half metals and opens opportunities for nanoscale highly efficient antiferromagnetic spintronics for information processing and storage.

2D materials | 2D magnetism | half metallicity | spin field effect transistor | antiferromagnetic spintronics

Scaling down of spintronic devices requires the precise knowledge and delicate control of magnetic properties of materials in reduced dimensions. Two-dimensional magnetic van der Waals (vdW) crystals (1–14), owing to their high crystallinity and atomic thinness and flatness, innately eliminate the challenges associated with the conventional thin-film preparation process, in which extrinsic defect or surface states and spurious magnetic anisotropies would be otherwise inevitable. Our recent experimental discovery of intrinsic ferromagnetism in 2D vdW crystals revealed the prominent dimensionality effect and the unusual magnetic field effect in the emerging magnetic properties of clean 2D vdW ferromagnets (3). Given the fact that there is much more abundance of antiferromagnetic vdW crystals with generally higher magnetic-order temperatures than ferromagnetic vdW crystals, as well as their robustness against environmental magnetic field perturbation and null stray fields (9–13, 15), 2D antiferromagnets would be significant in both fundamental physics and technological applications.

Despite the vanishing macroscopic magnetic moments, Néel (16) noted that antiferromagnets would be equivalent to ferromagnets for effects that are even functions of the magnetic moment. This notion has been applied in the recent resurgence of antiferromagnetic spintronics (17, 18), which are primarily based on spin-orbit interaction effects such as anisotropic magnetoresistance (19–21). It appears that antiferromagnetic spintronics applications

are moment-parity constrained. However, net magnetization should not be a fundamental limiting factor, for spin current relies solely on the concentration and polarization of electrons dwelling in proximity to the Fermi surface rather than on all electrons in the solids. In other words, it is theoretically rational that in a zero-magnetization system, conduction electrons remain polarized in spin degree of freedom. One intriguing class of examples that display this characteristic is antiferromagnetic half metals (22, 23), which have fully compensated magnetization yet completely spin-polarized electrons in conduction.

The scarcity of antiferromagnetic half metals demands the delicate design of complex materials such as Mn_3Al, Mn_3Ga (24), and VFeSb doped with Mn and In (25), the resultant stoichiometry and low defect density of which are also stringently required. Of tremendous value would be a rational design of half metallicity in simple and clean crystals. Realizing half metallicity, especially in materials of reduced dimensions, demands even more due to the almost inevitable spin-mixed surface or edge states caused by structural imperfections (26–28). We propose here that antiferromagnetic coupling of regions of ferromagnetic states offers intriguing platforms in which half metallicity can be brought forth by applying electric fields across the regions. Fig. 1A schematically illustrates the spin- and layer-resolved density of states for a bilayer
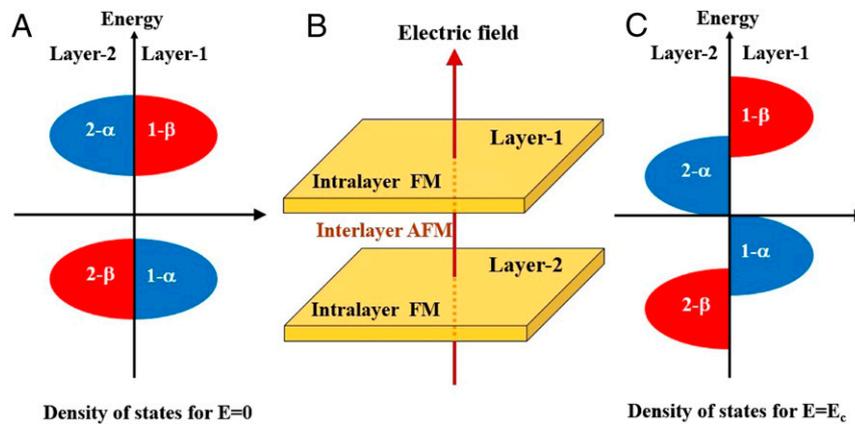
Fig. 1. (*A* and *C*) The schematic spin- and layer-resolved density of states of the A-type antiferromagnetic bilayer system with the electric field normal to the van der Waals plane (*A*) E = 0 and (*C*) E = E$_c$ (E$_c$ is the critical electric field for the emergence of half metallicity), in which 1-α(β) and 2-α(β) indicate the spin-α(β) channel in layer 1 and layer 2, respectively. (*B*) The schematic view of the A-type antiferromagnetic bilayer system with the perpendicular electric field pointing from layer 2 to layer 1.

A-type antiferromagnet, which exhibits an intralayer ferromagnetic order and interlayer antiferromagnetic order, as shown in Fig. 1*B*. In layer 1, spin-β electrons are of higher energy than spin-α electrons, and the order is inverted in layer 2. By applying an electric field penetrating from layer 2 to layer 1 (defined as the positive field), electrons of both spins in layer 1 (2) increase (decrease) in energy. Upon a critical field E$_c$, the energy band of spin-α electrons in layer 1 touches that of electrons with the same spin orientation in layer 2, leading to a merged metallic band with pure spin-α polarization at the Fermi level; that is, half metallicity emerges, as shown in Fig. 1*C*. While the electric field orientation is reversed, half metallicity would emerge with pure spin-β polarization.

Recently, a new type of single-layer ferromagnetic semiconductor in transition-metal dichalcogenides 2H-VX$_2$ (X = S, Se, and Te) has attracted great attention (29, 30). For bilayer 2H-VSe$_2$, the intralayer is still ferromagnetic, while the interlayer magnetic coupling is found to be antiferromagnetic (8, 30); i.e., bilayer 2H-VSe$_2$ is an A-type antiferromagnetic semiconductor. In the following, we use bilayer 2H-VSe$_2$ as an example to demonstrate the formation of the half metallicity induced by the cross-layer electric field. Our calculations are performed within density-functional theory (DFT) by the projector-augmented wave (PAW) method implemented in the Vienna ab initio simulation package (VASP), and the generalized gradient approximation (GGA) is used (31). The energy cutoff of 500 eV is used for the plane-wave basis expansion with the total energy convergence

criterion of 1×10^{-6} eV per unit cell. A Γ-centered k-grid $20 \times 20 \times 1$ is used to sample the 2D Brillouin zone. The convergence of energy with respect to number of k points and energy cutoff has been tested. For geometry optimization, all of the internal coordinates are relaxed until the Hellmann–Feynman forces are less than 1 meV/Å. The dispersion-corrected DFT-D2 method (32) is introduced in the first-principles calculations to relax the structure of the bilayer system. A large enough vacuum thickness (20 Å) along the z axis is adopted to avoid the interaction between adjacent unit cells.

The side view of the atomic structure of the bilayer 2H-VSe$_2$ is shown in Fig. 2*A*, in which the electric field indicated by the red arrow is applied perpendicularly to the 2D plane, pointing from layer 2 to layer 1. The optimized lattice constant is 3.335 Å, and the interlayer distance between the two Se layers is 3.220 Å, which agree well with previous studies (29). No electrodes are included in the calculations. To focus on the influence of the electric field, we do not do further structural relaxation for different electric fields, which is a reasonable approximation according to the test results (*SI Appendix*, Fig. S1) and our previous investigations (33, 34).

Our spin-polarized total energy calculations show that the ground-state configuration of single-layer VSe$_2$ is magnetic, which is reasonable as each V^{4+} ion has one unpaired electron. The magnetic coupling strength is strong, evidenced by the energy difference of 165 meV per V^{4+} ion for spin-polarized configuration vs. spin-unpolarized configuration. The magnetic anisotropy
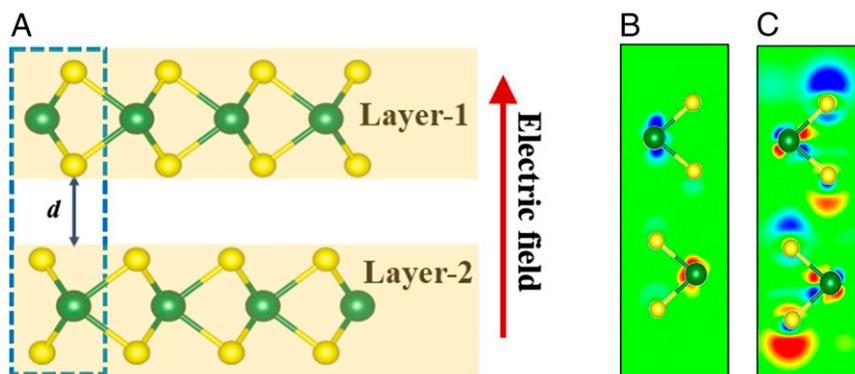
Fig. 2. (*A*) The side view of the bilayer 2H-VSe$_2$, with the electric field applied perpendicularly from layer 2 to layer 1. (*B* and *C*) The electric field-induced spin densities $\Delta\sigma = \sigma(E) - \sigma(0)$ and charge densities $\Delta\rho = \rho(E) - \rho(0)$ in arbitrary units under the influence of the electric field E = 0.8 V/Å. Red and blue colors in *B* represent the increase and decrease of the integrated spin-α electron densities, while in *C* they represent the accumulation and depletion of electrons, respectively.

Fig. 3. (*A–F*) Orbital- and spin-resolved band structures of bilayer 2H-VSe$_2$ with (*A* and *B*) E = 0, (*C* and *D*) E = E$_c$ = 0.4 V/Å, (*E* and *F*) E = 0.8 V/Å, (*A*, *C*, and *E*) spin-α, and (*B*, *D*, and *F*) spin-β. With a positive electric field applied, all layer-2–related bands (in yellow and green) are pushed down while layer-1 bands (in blue and red) are lifted up. After reaching the crit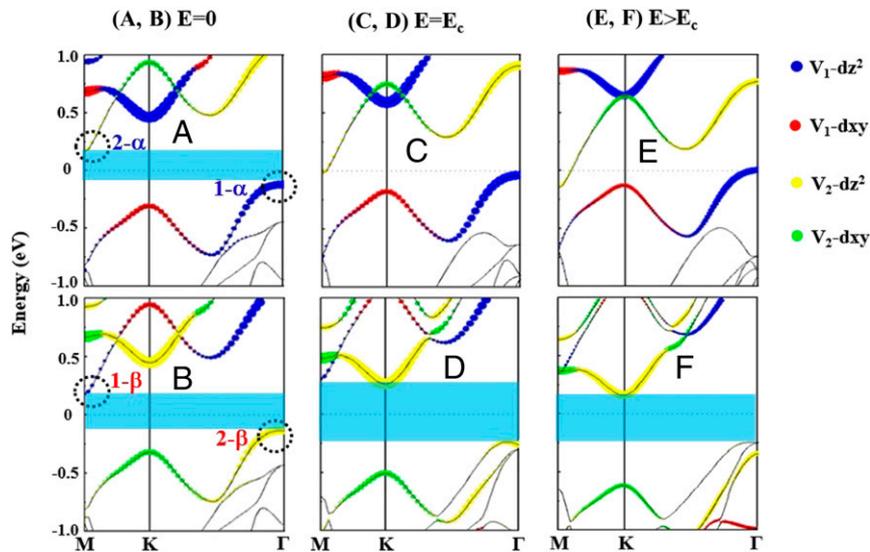ical field, the band edges in spin-α states touch at M-Γ (*C*), whereas the band edges in spin-β states separate farther apart and evolve from M-Γ (*B*) to K-Γ (*F*).

energy calculation shows the easy-plane magnetization in single-layer VSe$_2$, with 0.6 meV lower energy per V^{4+} ion than easy-axis (normal to the layer) ferromagnetic configuration, consistent with the previous report (29). While two layers are in contact, the interlayer antiferromagnetic coupling is energetically favorable, which is confirmed by calculations with GGA plus on-site Coulomb interaction U and with hybrid functional Heyd–Scuseria–Ernzerhof (HSE) approximation (35) (*SI Appendix,* Table S1). All of the quantitative data presented in this paper are calculated by the GGA+U scheme with U = 2 eV and J = 0.84 eV, unless noted otherwise. In 2D layered A-type antiferromagnets, the interlayer antiferromagnetic exchange interaction is usually much weaker than the intralayer ferromagnetic interaction. Although the interlayer exchange integral $J_\perp$ is small, the effective exchange interaction $NJ_\perp$ can be very large, where N is number of spins in the individual layer in the domain size. It means that there exists long correlation length along the z direction, once the intralayer ferromagnetic order is formed.

In Fig. 2B, we present the electric field-induced spin densities Δσ = σ(E) − σ(0) in arbitrary unit under the electric field E = 0.8 V/Å,

in which red and blue colors represent the increase and decrease of the integrated spin-α electron densities. The induced spin density analysis confirms that the evolution of magnetization primarily occurs on vanadium atoms. The spin-α density of layer 1 is decreased, and that of layer 2 is increased, which agrees with the schematic trend in Fig. 1C. The asymmetry of induced spin densities on vanadium atoms in two layers are caused by different orbital compositions at conduction and valence band edges, which are shown in Fig. 3. In Fig. 2C, we show the charge densities Δρ = ρ(E) − ρ(0) with the same conditions as in Fig. 2B, in which red and blue colors represent the increase and decrease of the integrated electron densities. From the induced charge density, we can see that opposite charges are induced in the two layers, and due to the screening effect, the induced charges are mainly located on the outermost selenium atoms.

Orbital- and spin-resolved band structures of bilayer 2H-VSe$_2$ shown in Fig. 3 exhibit four major features: (*i*) Bilayer 2H-VSe$_2$ is a semiconductor with an indirect gap 0.3 eV, smaller than the value from HSE calculations (*SI Appendix,* Fig. S2); (*ii*) electronic bands are spin polarized within each layer, agreeing with
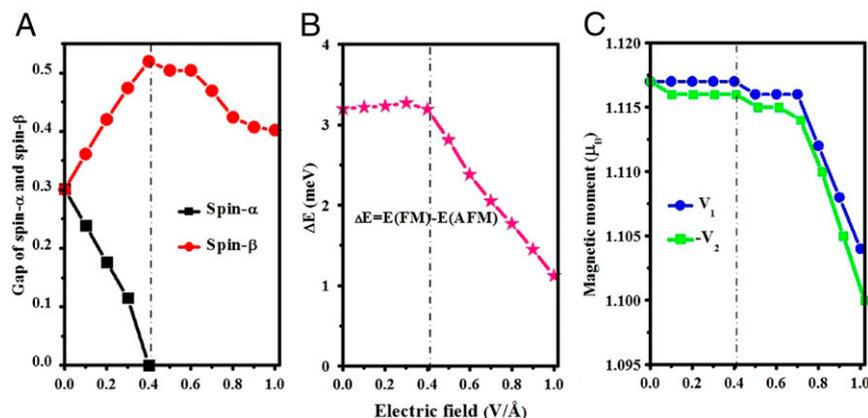

Fig. 4. (*A–C*) Electric field dependence of (*A*) the band gap of spin-α and spin-β states, (*B*) energy difference between ferromagnetic and antiferromagnetic interlayer coupling, and (*C*) the magnetic moments of V$_1$ and V$_2$. The critical field (0.4 V/Å) is indicated by a dashed-dotted line.
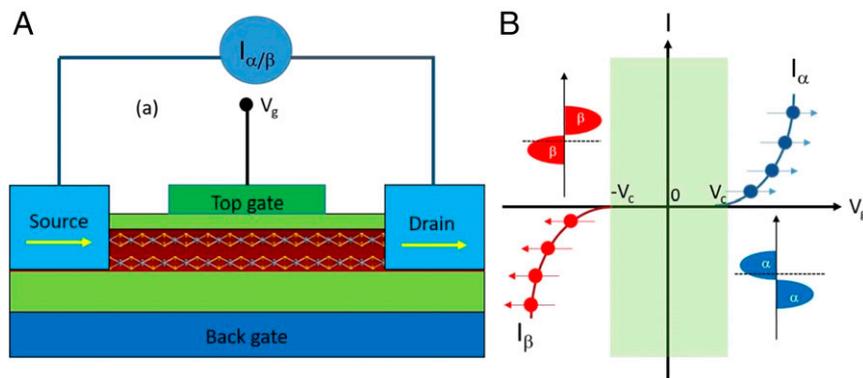
Fig. 5. (*A*) The schematic structure of the proposed spin field effect transistor based on the 2D antiferromagnetic half metals. The gate voltage V_g is applied to control the spin states in the channel. (*B*) The schematic spin-polarized current vs. the gate voltage, with V_c indicating the critical voltage. The switching of the spin-α current I_α and spin-β current I_β can be manipulated by the gate voltage.

the intralayer ferromagnetic order (29, 36–38); (*iii*) between layers, the order of spin orientations is opposite, coinciding with the interlayer antiferromagnetic coupling; and (*iv*) valence band edges are mainly composed of d_{z^2} orbitals and conduction band edges are composed of d_{z^2} and $d_{x^2-y^2}/d_{xy}$ orbitals. The light blue regions in Fig. 3 indicate the band gap of the spin-α (Fig. 3, *Top*) and spin-β (Fig. 3, *Bottom*) channels. When the electric field is absent, the band gaps of spin-α and spin-β are equal, as shown in Fig. 3 *A* and *B*. When applying the critical electric field E_c (0.4 V/Å), we can clearly see the gap closure for the spin-α channel and the gap opening for the spin-β channel. When the electric field becomes larger than E_c (Fig. 3 *E* and *F*), the spin-α channel becomes metallic and the spin-β channel keeps insulating; i.e., the half metallicity appears. Although all our present results are based on bilayer VSe_2, multilayers with an even layer number may also work. We check the band structures of four and six layers of VSe_2 (*SI Appendix*, Fig. S3) and notice that the band gap of vdW thin films may decrease with the increasing layer numbers (39), which may result in the semiconductor–metal transition. The metallic multilayer does not work in our scheme.

We plot the electric field dependence of the band gap of the spin-α and spin-β channels in Fig. 4*A*, in which we can see that bilayer VSe_2 keeps the half metallicity when the applied electric field is larger than the critical field. In the whole range of the 0 ~ 1.0 V/Å electric field, the total energy calculation shows the ground state of interlayer coupling remains antiferromagnetic (Fig. 4*B*). Before reaching the critical field and the band crossing, in 0-K ground state calculations, the applied field induces intralayer electronic polarization, but does not cause interlayer charge transfer. Therefore, the net magnetic moment within each layer is not noticeably altered, yet slight reduction of magnetic moments can still arise from the intralayer charge redistribution between different orbitals as a response of small fields (Fig. 4*C*). After forming the metallic state, as the degree of band crossing increases, effective charge transfer (i.e., spin compensation) occurs between layers. The net magnetization of each layer drops, for example, at 1.0 V/Å, from 1.117 μ_B at zero field to 1.104 μ_B for V_1 and from −1.117 μ_B at zero field to −1.099 μ_B for V_2, equal to a reduction of 1.35×10^{13} cm^{-2} and 1.87×10^{13} cm^{-2} spin-polarized carriers per layer, respectively. This analysis suggests the electric field as an effective knob to tune the density of spin-polarized carriers for nanoscale spintronic device applications.

After band crossing, although the whole bilayer system remains charge neutral, the individual constituent layers undergo doping effects via interlayer charge transfer. Interestingly, the available unoccupied states in one layer and the transferred electrons from the other layer have the same spin orientation. Therefore, interlayer charge transfer gradually increases the

weight of interlayer ferromagnetic coupling. Furthermore, before forming the metallic band, the interlayer antiferromagnetic coupling is established by super-superexchange through intermediate "-Se Se-." However, with the applied field, the enhanced degree of metallicity would involve an increasing population of conduction electrons as the media for the indirect exchange coupling between interlayer vanadium ions, which possibly results in ferromagnetic coupling as seen in a variety of conductive systems such as diluted magnetic semiconductors, graphene nanoribbon, etc. (40–44). Our calculations confirm the trend inferred from the above analysis that, for U = 1 eV (stronger screening and more metallic), the critical field for half metallicity is 0.3 V/Å, and the interlayer ferromagnetism is established upon the field of 0.4 V/Å (*SI Appendix*, Fig. S4); for U = 2 eV (relatively weaker screening and more localization), a larger electric field (~1.5 V/Å) is required for establishing the interlayer ferromagnetism.

For the ground state of this closed bilayer system (without electrodes for sourcing and draining charges) discussed above, there is no gate-induced doping and the whole system is kept neutral. The neutrality efficiently enables field-induced energy shifts of equal magnitude yet opposite signs on band structures of two constituent layers. Therefore, half metallicity with 100% spin-α conduction electrons is effectively generated as a result of the gap closing of one spin-polarized band and the gap widening of the other one while the critical field 0.4 V/Å is reached, as shown in Fig. 3*C*. Reversing the electric field orientation switches the polarity of the half metal to carry 100% spin-β conduction electrons. Hence, in analogy to conventional semiconductor transistors, the vertical electric field can act as a "gate" to switch the half metallicity as well as control its polarity. However, the fundamental mechanism is entirely distinct, as such a spin field effect transistor (FET) (45) operates purely via the band structure engineering, in contrast to the working principle of traditional transistors by modulating charge populations. A practical remark on the open system while source and drain electrodes are integrated for circuitry is as follows (Fig. 5*A*): Due to the gating effect, the Fermi level of the bilayer VSe_2 would be pushed into the conduction or valence band (Fig. 5*B*, *Inset*) while positive or negative critical fields (voltages) are applied. The field-induced doping enables an enhanced conductivity of the half-metallic bilayer VSe_2.

We also tracked the evolution of the magnetic anisotropy energy in the whole range of applied electric fields. Magnetic anisotropy energy not only reveals the preferred ground-state magnetization orientation, but also suggests the relative robustness of the long-range magnetic order against thermal excitations at finite temperatures (3). Our calculations show the decreasing

in-plane magnetic anisotropy energy with the increasing field strength (*SI Appendix*, Fig. S5). In fact, it would be even more intriguing if the electric field could reorient the spin vector normal to the plane, for easy-axis magnetic anisotropy can stabilize the long range magnetic order in 2D systems at finite temperatures and perpendicular magnetization can benefit ultrahigh-density data storage (46). Although a moderate electric field for establishing easy-axis magnetization in bilayer VSe_2 is not gained, it is meaningful to note that quantitative values herein such as critical field and magnetic anisotropy vary in materials, depending on band gap size, spin-orbit coupling strength, crystal structure, and constituent elements, etc. This leaves room for material selections.

Although our work provides a general route for exploring half metallicity based on 2D A-type antiferromagnetic bilayers, it is necessary to point out the following: (*i*) The Mermin–Wagner theorem predicts that a 2D isotropic Heisenberg system does not have long-range magnetic order at finite temperatures (47). However, the uniaxial magnetic anisotropy (48) can break the hypothesis of the Mermin–Wagner theorem and the long-range dipolar coupling (49) can cause domain formation. According to the previous report and our theoretical confirmation, 2H-VSe_2 belongs to the family of 2D *XY* magnets (30). The long-range dipolar spin–spin correlation can stabilize the magnetic order in a finite size in 2D *XY* magnets (50–52). The typical domain size in the layered 2D *XY* magnets on the order of 100 Å (50) promises its application in nanoscale spintronic devices. Domain size is an important consideration in realizing 2D spin FET based on the scheme proposed in this work. (*ii*) Results in this work based on bilayer 2H-VSe_2 can be applicable qualitatively to other small-bandgap bilayer A-type antiferromagnets. Before experimental endeavors toward half metallicity and spin FET proposed in this work, one should carefully examine the crystalline structure, band structure, and magnetic ground state of the material system. More A-type antiferromagnetic semiconductors will be found or designed with the rapid development of the 2D magnetic materials, which will accelerate the experimental realization of the 2D half metallicity. Recently, the layer-contrasting observation in CrI_3 (4) indicated that the interlayer magnetic coupling may be antiferromagnetic, which still needs further efforts to clarify the exact ground-state magnetic configurations and the role of graphite encapsulation in the resultant magnetic properties. In light of practical considerations discussed above, the half metallicity produced by the 2D A-type antiferromagnetic semiconductor with the assistance of the electric field will be of great practical significance in the 2D spintronic devices.

1. Bonilla M, et al. (2018) Strong room-temperature ferromagnetism in VSe_2 monolayers on van der Waals substrates. *Nat Nanotechnol* 13:289–293.
2. Park J-G (2016) Opportunities and challenges of 2D magnetic van der Waals materials: Magnetic graphene? *J Phys Condens Matter* 28:301001.
3. Gong C, et al. (2017) Discovery of intrinsic ferromagnetism in two-dimensional van der Waals crystals. *Nature* 546:265–269.
4. Huang B, et al. (2017) Layer-dependent ferromagnetism in a van der Waals crystal down to the monolayer limit. *Nature* 546:270–273.
5. O'Hara DJ, et al. (2018) Room temperature intrinsic ferromagnetism in epitaxial manganese selenide films in the monolayer limit. *Nano Lett* 18:3125–3131.
6. Zhuang HL, Hennig RG (2016) Stability and magnetism of strongly correlated single-layer VS_2. *Phys Rev B* 93:054429.
7. Zhou Y, et al. (2012) Tensile strain switched ferromagnetism in layered NbS_2 and $NbSe_2$. *ACS Nano* 6:9727–9736.
8. Tong W-Y, Duan C-G (2017) Electrical control of the anomalous valley Hall effect in antiferrovalley bilayers. *npj Quantum Mater* 2:47.
9. Chittari BL, et al. (2016) Electronic and magnetic properties of single-layer MPX_3 metal phosphorous trichalcogenides. *Phys Rev B* 94:184428.
10. Le Flem G, Brec R, Ouvard G, Louisy A, Segransan P (1982) Magnetic interactions in the layer compounds MPX_3 (M = Mn, Fe, Ni; X = S, Se). *J Phys Chem Solids* 43:455–461.
11. McGuire MA, et al. (2017) Antiferromagnetism in the van der Waals layered spin-lozenge semiconductor $CrTe_3$. *Phys Rev B* 95:144421.
12. Wildes AR, et al. (2015) Magnetic structure of the quasi-two-dimensional antiferromagnet $NiPS_3$. *Phys Rev B Condens Matter Mater Phys* 92:224408.
13. Ressouche E, et al. (2010) Magnetoelectric $MnPS_3$ as a candidate for ferrotoroidicity. *Phys Rev B Condens Matter Mater Phys* 82:100408.
14. Son Y-W, Cohen ML, Louie SG (2006) Half-metallic graphene nanoribbons. *Nature* 444:347–349.
15. Li X, Cao T, Niu Q, Shi J, Feng J (2013) Coupling the valley degree of freedom to antiferromagnetic order. *Proc Natl Acad Sci USA* 110:3738–3742.
16. Néel L (1971) Magnetism and local molecular field. *Science* 174:985–992.
17. Jungwirth T, Marti X, Wadley P, Wunderlich J (2016) Antiferromagnetic spintronics. *Nat Nanotechnol* 11:231–241.
18. MacDonald AH, Tsoi M (2011) Antiferromagnetic metal spintronics. *Philos Trans A Math Phys Eng Sci* 369:3098–3114.
19. Železný J, et al. (2014) Relativistic Néel-order fields induced by electrical current in antiferromagnets. *Phys Rev Lett* 113:157201.
20. Shick AB, Khmelevskyi S, Mryasov ON, Wunderlich J, Jungwirth T (2010) Spin-orbit coupling induced anisotropy effects in bimetallic antiferromagnets: A route towards antiferromagnetic spintronics. *Phys Rev B Condens Matter Mater Phys* 81:212409.
21. McGuire T, Potter R (1975) Anisotropic magnetoresistance in ferromagnetic 3d alloys. *IEEE Trans Magn* 11:1018–1038.
22. de Groot RA (1991) Half-metallic magnetism in the 1990s. *Physica B* 172:45–50.
23. Hu X (2012) Half-metallic antiferromagnet as a prospective material for spintronics. *Adv Mater* 24:294–298.
24. Gao GY, Yao K-L (2013) Antiferromagnetic half-metals, gapless half-metals, and spin gapless semiconductors: The D03-type Heusler alloys. *Appl Phys Lett* 103:232409.
25. van Leuken H, de Groot RA (1995) Half-metallic antiferromagnets. *Phys Rev Lett* 74:1171–1173.
26. Li Y, Zhou Z, Shen P, Chen Z (2009) Spin gapless semiconductor-metal-half-metal properties in nitrogen-doped zigzag graphene nanoribbons. *ACS Nano* 3:1952–1958.
27. Jiao L, Wang X, Diankov G, Wang H, Dai H (2010) Facile synthesis of high-quality graphene nanoribbons. *Nat Nanotechnol* 5:321–325.
28. Zheng F-L, Zhang Y, Zhang J-M, Xu K-W (2011) Effect of the dangling bond on the electronic and magnetic properties of BN nanoribbon. *J Phys Chem Solids* 72:256–262.
29. Fuh H-R, et al. (2016) Newtype single-layer magnetic semiconductor in transition-metal dichalcogenides VX_2 (X = S, Se and Te). *Sci Rep* 6:32625.
30. Esters M, Hennig RG, Johnson DC (2017) Dynamic instabilities in strongly correlated $VSe2$ monolayers and bilayers. *Phys Rev B* 96:235147.
31. Perdew JP, Burke K, Ernzerhof M (1996) Generalized gradient approximation made simple. *Phys Rev Lett* 77:3865–3868.
32. Grimme S (2006) Semiempirical GGA-type density functional constructed with a long-range dispersion correction. *J Comput Chem* 27:1787–1799.
33. Yao Q-F, et al. (2017) Manipulation of the large Rashba spin splitting in polar two-dimensional transition-metal dichalcogenides. *Phys Rev B* 95:165401.
34. Gong S-J, Duan C-G, Zhu Y, Zhu Z-Q, Chu J-H (2013) Controlling Rashba spin splitting in Au(111) surface states through electric field. *Phys Rev B Condens Matter Mater Phys* 87:035403.
35. Heyd J, Scuseria GE, Ernzerhof M (2003) Hybrid functionals based on a screened Coulomb potential. *J Chem Phys* 118:8207–8215.
36. Tong W-Y, Gong S-J, Wan X, Duan C-G (2016) Concepts of ferrovalley material and anomalous valley Hall effect. *Nat Commun* 7:13612.
37. Ma Y, et al. (2012) Evidence of the existence of magnetism in pristine VX_2 monolayers (X = S, Se) and their strain-induced tunable magnetic properties. *ACS Nano* 6:1695–1701.
38. Wasey AHMA, Chakrabarty S, Das GP (2015) Quantum size effects in layered VX_2 (X = S, Se) materials: Manifestation of metal to semimetal or semiconductor transition. *J Appl Phys* 117:064313.
39. Kuc A, Zibouche N, Heine T (2011) Influence of quantum confinement on the electronic structure of the transition metal sulfide TS_2. *Phys Rev B Condens Matter Mater Phys* 83:245213.
40. Kan E-J, Li Z, Yang J, Hou JG (2007) Will zigzag graphene nanoribbon turn to half metal under electric field? *Appl Phys Lett* 91:243116.
41. Shen L, et al. (2008) Charge-transfer-based mechanism for half-metallicity and ferromagnetism in one-dimensional organometallic sandwich molecular wires. *J Am Chem Soc* 130:13956–13960.
42. Wu M, Zhang Z, Zeng XC (2010) Charge-injection induced magnetism and half metallicity in single-layer hexagonal group III/V (BN, BP, AlN, AlP) systems. *Appl Phys Lett* 97:093109.
43. Ye L-H, Freeman AJ, Delley B (2006) Half-metallic ferromagnetism in Cu-doped ZnO: Density functional calculations. *Phys Rev B Condens Matter Mater Phys* 73:033203.
44. Li X, Wu X, Yang J (2014) Half-metallicity in $MnPSe_3$ exfoliated nanosheet with carrier doping. *J Am Chem Soc* 136:11065–11069.
45. Datta S, Das B (1990) Electronic analog of the electro-optic modulator. *Appl Phys Lett* 56:665–667.
46. Weller D, Moser A (1999) Thermal effect limits in ultrahigh-density magnetic recording. *IEEE Trans Magn* 35:4423–4439.

APPLIED PHYSICAL SCIENCES

47. Mermin ND, Wagner H (1966) Absence of ferromagnetism or antiferromagnetism in one- or two-dimensional isotropic Heisenberg models. *Phys Rev Lett* 17:1133–1136.
48. Bander M, Mills DL (1988) Ferromagnetism of ultrathin films. *Phys Rev B Condens Matter* 38:12015–12018.
49. Berezinskii VL, Ya Blank A (1973) Thermodynamics of layered isotropic magnets at low temperatures. *Zh Eksp Teor Fiz* 64:725–740.
50. Bramwell ST, Holdsworth PCW (1993) Magnetization and universal sub-critical behaviour in two-dimensional XY magnets. *J Phys Condens Matter* 5:L53.
51. Bramwell ST, Holdsworth PCW (1994) Magnetization: A characteristic of the Kosterlitz-Thouless-Berezinskii transition. *Phys Rev B Condens Matter* 49:8811–8814.
52. Elmers HJ, Hauschild J, Liu GH, Gradmann U (1996) Critical phenomena in the two-dimensional XY magnet Fe(100) on W(100). *J Appl Phys* 79:4984–4986.